SCIENTIFIC REPORTS

OPEN

Received: 07 January 2016
Accepted: 01 March 2016
Published: 21 March 2016

23327Enhanced photoelectric conversion efficiency of dye-sensitized solar cells by the incorporation of flower-like Bi_2S_3:Eu^{3+} sub-microspheres

Bingyu Xu, Guofeng Wang & Honggang Fu

In this paper, TiO_2-Bi_2S_3 and TiO_2-Bi_2S_3:Eu^{3+} composite photoanodes were successfully designed, which can not only fully absorb visible light but also transfer the electron from Bi_2S_3 to TiO_2 conduction band due to the narrow band gap and high conduction band of Bi_2S_3. Compared to pure TiO_2 cell, the photoelectric conversion efficiencies of TiO_2-Bi_2S_3 and TiO_2-Bi_2S_3:Eu^{3+} composite cells were increased significantly. In addition, the efficiency of TiO_2-Bi_2S_3:Eu^{3+} composite cells were higher than that of TiO_2-Bi_2S_3 cell which could be attributed to the larger BET surface area of Bi_2S_3:Eu^{3+}. The electron transport and interfacial recombination kinetics were investigated by the electrochemical impedance spectroscopy and intensity-modulated photocurrent/photovoltage spectroscopy. The results indicated that the interfacial resistance of the TiO_2-dye|I_3^-/I^- electrolyte interface of TiO_2-Bi_2S_3:Eu^{3+} composite cell was much bigger than that of pure TiO_2 cell. In addition, the TiO_2-Bi_2S_3:Eu^{3+} cell has longer electron recombination time and longer electron transport time than pure TiO_2 cell. The charge collection efficiency of TiO_2-Bi_2S_3:Eu^{3+} composite cell was higher than that of pure TiO_2 cell.

In the past decade, dye-sensitized solar cells (DSSCs) have attracted extensive attention due to their easy fabrication, lowcost and relatively high conversion efficiency[1,2]. A typical DSSC consists of a dye-sensitized semiconductor photoanode, an electrolyte with the dissolved iodide/triiodide (I_3^-/I^-) redox couple between the electrodes and a catalytic counter electrode[3–6]. Especially, an advanced photoelectrode is one of the most important prerequisites for highly efficient DSSCs. A variety of materials have been used as photoelectrodes and show good electrocatalytic activity. In general, TiO_2 has been widely used as for DSSCs owing to their large surface area for loading more dye molecules, the sensitizer of the DSSC is mainly N719 dye, and the DSSC consists of TiO_2 film sensitized by a dye for absorbing incident light. Recently, extensive studies on the individual components of DSSCs have been performed to further reduce production costs and to achieve better cell performance[7–9]. Many attempts have been made to enhance the performances of DSSCs by controlling the size, shape and morphologies of the semiconductors, utilizing low band gap organic materials, introducing buffer layers, and so on. Among them, one facile and efficient approach is to introduce foreign ions into organic semiconductors[10,11]. Some metal oxides[12,13], nitrides[14], carbides[15] and sulfides[16–19] have also been investigated as CEs due to their preferentially electrocatalytic activity. However, the application of sulfides as photoanode has been seldom reported. Metal sulfides gained more attention due to their facile preparation conditions and relatively low toxicity. As a well-known semiconductor, bismuth sulfide (Bi_2S_3) has the potential to improve the photocatalytic activity due to its narrow bandgap (~1.4 eV)[20,21]. It could has been used as a photoanode materials in DSSC due to its ability to absorb a large part of visible light up to 800 nm and transfer the electron from Bi_2S_3 to TiO_2 conduction band. So far, there are many classic preparation methods for Bi_2S_3, such as hydrothermal method, solvothermal method, electrochemical deposition, microwave refluxing, organometallic complex decomposition and chemical vapor deposition[22–28].

Key Laboratory of Functional Inorganic Material Chemistry, Ministry of Education, School of Chemistry and Materials Science, Heilongjiang University, Harbin, 150080, China. Correspondence and requests for materials should be addressed to G.W. (email: wanggf_w@163.com) or H.F. (email: fuhg@vip.sina.com)

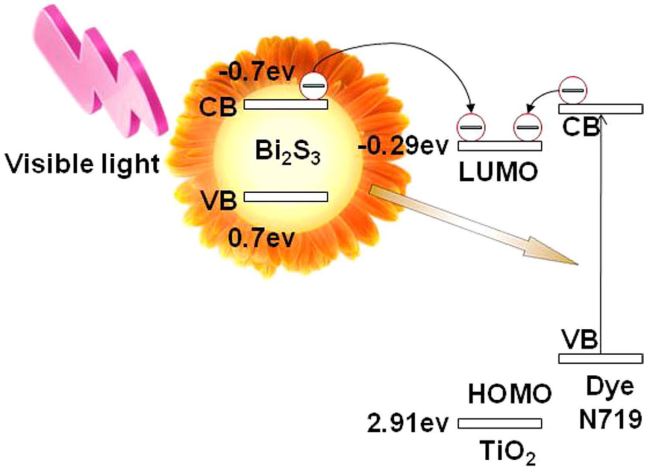

Figure 1. Mechanism of visible light harvesting in TiO_2-Bi_2S_3:Eu^{3+} cells.

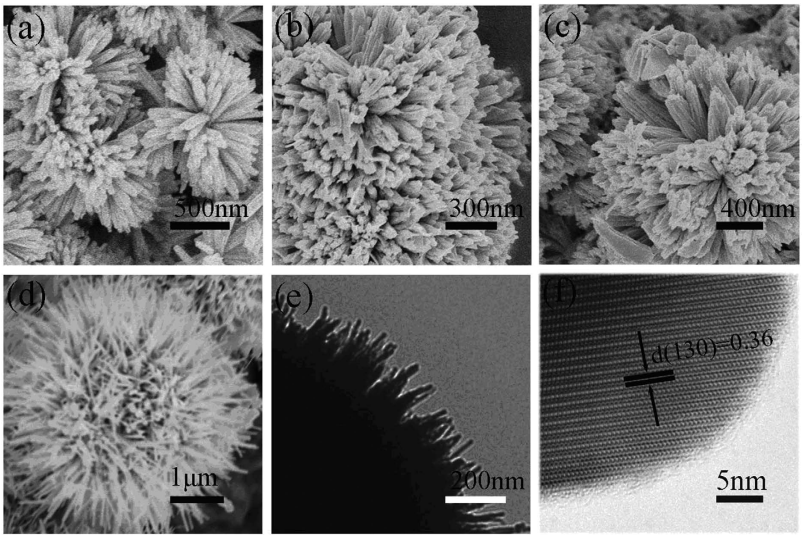

Figure 2. SEM (**a–d**), TEM and HRTEM (**e,f**) images of Bi_2S_3: Eu^{3+} nanocrystals prepared at 180 °C for 12h after annealing at 400 °C with different Eu^{3+} concentrations: (**a**) 5%, (**b**) 10%, (**c**) 15%, and (**d–f**) 20%.

As a result, if one can design down-conversion luminescent TiO_2-Bi_2S_3:Eu^{3+} composite photoanodes, not only the utilization of visible light can be improved but also the electron can transfer from Bi_2S_3 to TiO_2 conduction band (see Fig. 1). And thus, the efficiency of the solar cells can be enhanced. In addition, metal ions doping semiconductor is also an effective strategy to improve the photocatalytic performance. Based on the consideration above, we report the synthesis of flower-like Bi_2S_3:Eu^{3+} through a hydrothermal route, and introduce Bi_2S_3:Eu^{3+} to the dye-sensitized solar photoanodes. The BET surface areas increased with increasing Eu^{3+} concentration. The photoelectric conversion efficiencies of TiO_2-Bi_2S_3 and TiO_2-Bi_2S_3:Eu^{3+} composite cells were significantly increased compared to pure TiO_2 cell. The electron transport and interfacial recombination kinetics of cells were investigated in detail.

Discussion

Figure 2(a–d) represent the typical SEM images of the Bi_2S_3 products with different Eu^{3+} concentrations, which show that the products are composed of flower-like nanostructures. The average diameter of these superstructures is about 500 nm. The TEM and HRTEM images are presented in Fig. 2(e,f). The HRTEM image reveals that the interplanar spacing of 0.36 nm corresponds to the (130) plane of Bi_2S_3.

Figure 3 shows the XRD patterns of Bi_2S_3 nanocrystals (without annealing) with different reaction time, which are in good agreement with the standard data of orthorhombic phase Bi_2S_3 (JCPDS 17-0320). No other impurity peaks were detected. Figure 4 shows the XRD patterns of Bi_2S_3 nanocrystals after annealing at different temperatures. It can be seen crystalline size increases with increasing the annealing temperature. The peaks in Fig. 4 marked by asterisk (*) arise from cubic phase Bi particles (JCPDS 44-1256). The other diffraction peaks can be indexed to the orthorhombic phase Bi_2S_3. Figure 5 shows the XRD pattern of Bi_2S_3:Eu^{3+} nanocrystals (without

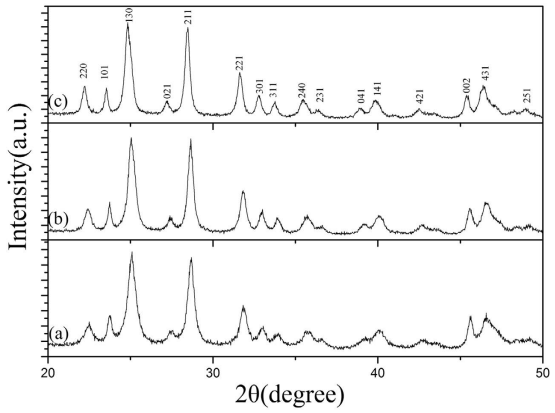

Figure 3. XRD patterns of Bi_2S_3: Eu^{3+} nanocrystals prepared at 180 °C for different reaction time: (**a**) 6 h, (**b**) 9 h, and (**c**) 12 h.

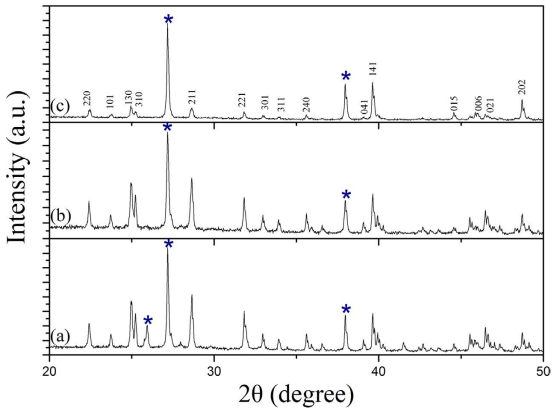

Figure 4. XRD patterns of Bi_2S_3: Eu^{3+} nanocrystals prepared at 180 °C for 12h with annealing at different temperatures for 2h: (**a**) 400 °C, (**b**) 600 °C, and (**c**) 800 °C.

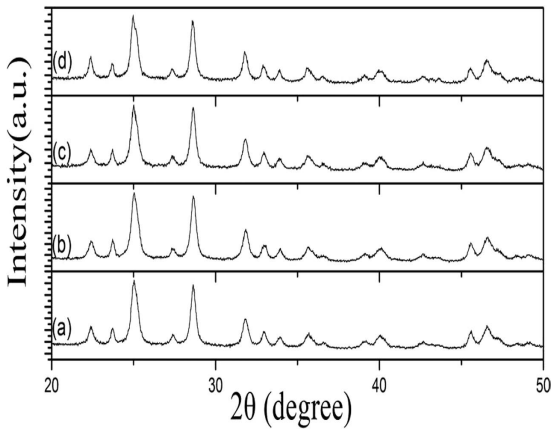

Figure 5. XRD patterns of Bi_2S_3:Eu^{3+} nanocrystals prepared at 180 °C for 12h with different Eu^{3+} concentrations: (**a**) 5%, (**b**) 10%, (**c**) 15%, and (**d**) 20%.

annealing) with different Eu^{3+} concentrations. Obviously, no other impurity peaks were detected with increasing Eu^{3+} concentration.

Figure 6 shows the Raman spectra of Bi_2S_3:Eu^{3+} with different Eu^{3+} concentrations. The typical features in Raman spectra were located at 129 cm^{-1}, 610 cm^{-1} and 965 cm^{-1}.The 610 and 965 cm^{-1} bands are assigned to the Bi-S stretching vibrations. The 129 cm^{-1} is attributed to the surface of the optical phonon modes[29].

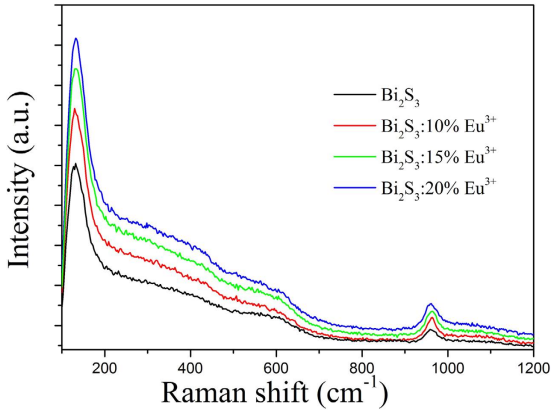

Figure 6. Raman spectra of Bi_2S_3:Eu^{3+} nanocrystals prepared at 180 °C for 12h with different Eu^{3+} concentrations.

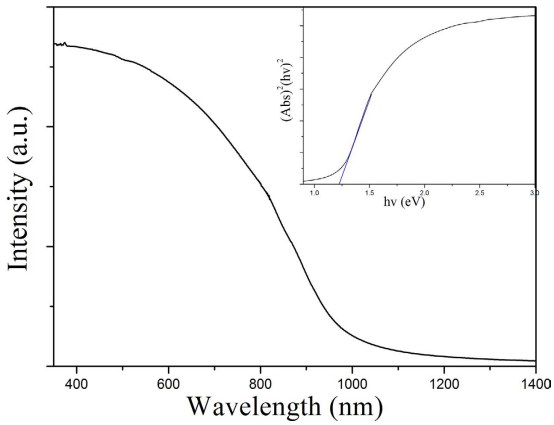

Figure 7. UV-Vis diffuse reflectance spectrum of Bi_2S_3 nanocrystals prepared at 180 °C for 12 h.

Figure 7 shows the UV-vis diffuse reflectance spectrum of Bi_2S_3 nanocrystals. The inset displays the plot of the transformed KubelkaeMunk function versus energy of light. The Kubelka-Munk function, F(R), allows the optical absorbance of a sample to be approximated from its reflectance: $F(R) = (1 - R)^2/2R$. For a semiconductor sample this allows the construction of a Tauc Plot-$(F(R).h)^n$ vs hv. For a direct band gap semiconductor the plot $n = 1/2$ will show a linear Tauc Region just above the optical absorption edge. Extrapolation of this line to the photon energy axis yields the semiconductor band gap. The calculated value of the band gap is about 1.22 eV for Bi_2S_3 nanocrystals.

In order to investigate the effects of TiO_2-Bi_2S_3:Eu^{3+} on the photoelectric properties of DSSCs, the DSSC prototype devices were fabricated by using N719-sensitised TiO_2-Bi_2S_3:Eu^{3+} composite electrodes. Figure 8(a) shows the photocurrent-voltage (I–V) curves of pure TiO_2 cell, TiO_2-Bi_2S_3 composite cell, and TiO_2-Bi_2S_3:Eu^{3+} cells. The mass concentrations of Bi_2S_3:Eu^{3+} in the TiO_2-Bi_2S_3:Eu^{3+} cells are 1%, 3%, and 5%, respectively. The corresponding values of the open-circuit voltage (V_{oc}), short-circuit current (J_{sc}), fillfactor (FF), and overall conversion efficiency (η), obtained from the curves of solar cells, are shown in Table 1. The result indicated that the photoelectric conversion efficiencies of the TiO_2-Bi_2S_3 and TiO_2-Bi_2S_3:Eu^{3+} composite cells were higher than that of pure TiO_2 cell. The best photoelectric conversion performance was observed when the mass concentration of Bi_2S_3:Eu^{3+} was 3%. The high Voc of the TiO_2-Bi_2S_3 could be attributed to heavy doping effects. Heavy impurity doping makes the conduction and valence bands shift, and brings about the so-called Band Gap Narrowing that resulting in the decrease of open circuit voltage. Figure 8(b) shows the incident photon to current (IPCE) spectra of pure TiO_2, TiO_2-Bi_2S_3, and TiO_2-Bi_2S_3:Eu^{3+} composite cells. The results indicated that the photon-to-current conversion efficiency obviously increases by the incorporation of Bi_2S_3:Eu^{3+}. With the increase of the proportion of Bi_2S_3:Eu^{3+} in TiO_2-Bi_2S_3:Eu^{3+} cell, the efficiency increases first, and then decreases. At low concentrations of Bi_2S_3:Eu^{3+}, the increase of the efficiency with the proportion of Bi_2S_3:Eu^{3+} could be attributed to the narrow band-gap and higher conduction band of Bi_2S_3, which not only improve the utilization of visible light but also transfer the electron from Bi_2S_3 to the conduction band of TiO_2. However, the incorporation of Bi_2S_3:Eu^{3+} can influence the electrical conductivity of TiO_2 and lead to a decrease in photocurrent. In addition, the effects of pure Bi_2S_3 on the photoelectric properties of DSSC were also studied. The results indicated that the photoelectric conversion efficiency of TiO_2-Bi_2S_3 cell was lower than that of TiO_2-Bi_2S_3:Eu^{3+} cell.

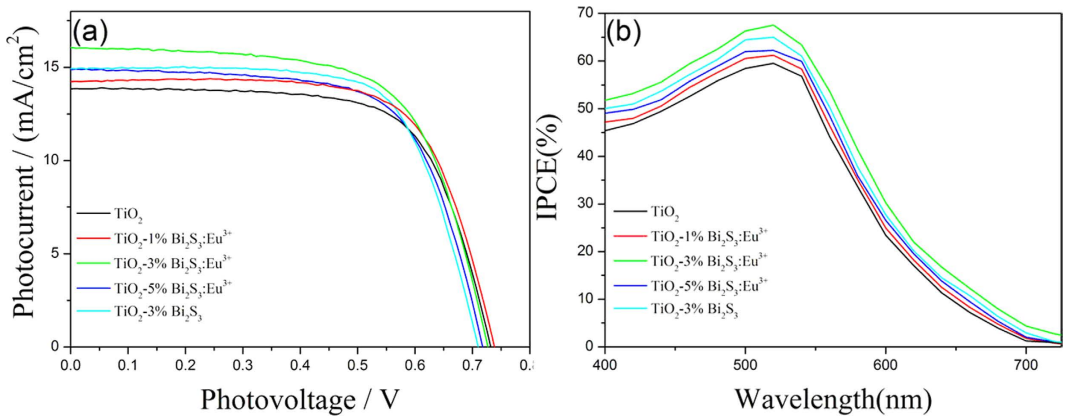

Figure 8. Photocurrent-voltage (I–V) curves (**a**) and IPCE (**b**) of TiO_2, TiO_2-Bi_2S_3, and TiO_2-Bi_2S_3:Eu^{3+} cells with different concentration of Bi_2S_3:Eu^{3+}.

Samples	I_{sc} (mA cm^{-2})	V_{oc} (V)	FF	η (%)
Pure TiO_2	13.0056	0.743	0.68	6.95
TiO_2-1%Bi_2S_3:Eu^{3+}	14.2333	0.739	0.69	7.29
TiO_2-3%Bi_2S_3:Eu^{3+}	16.0667	0.727	0.65	7.47
TiO_2-5%Bi_2S_3:Eu^{3+}	14.8667	0.718	0.67	7.10
TiO_2-3%Bi_2S_3	14.9333	0.711	0.69	7.33

Table 1. Solar cell parameters of TiO_2, TiO_2-Bi_2S_3, and TiO_2-Bi_2S_3:Eu^{3+} cells with different concents of Bi_2S_3:Eu^{3+}.

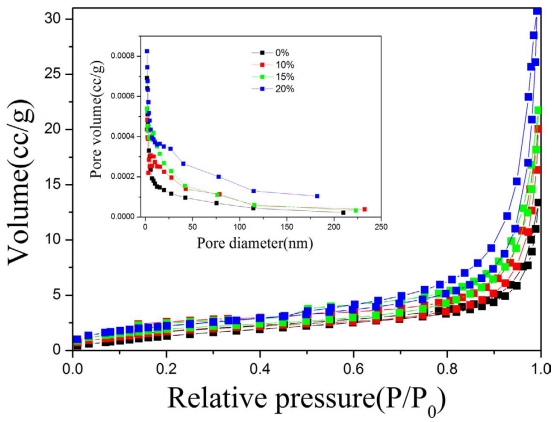

Figure 9. N_2 adsorption-desorption isotherm curves and pore size distribution (inset) of Bi_2S_3:Eu^{3+} nanocrystals prepared at 180 °C for 12 h with different Eu^{3+} concentrations.

It is well known that the photoelectric performance was closely related to the ratios of the surface areas of samples. N_2 adsorption-desorption isotherms and the corresponding BJH pore size distribution plots of the as-obtained Bi_2S_3:Eu^{3+} with different Eu^{3+} concentrations were performed to determine the surface area of the samples, as shown in Fig. 9. The BET surface areas are 4.8435, 5.4181, 6.6296, and 7.1739 m^2/g for 0%, 10%, 15%, and 20% Eu^{3+}, respectively.

EIS is a powerful method to investigate internal resistances for the charge-transfer process of DSSCs. The wide frequency range of EIS means that it can measure wide-scale internal resistances of each electrochemical step at the same time[30,31]. DSSCs are complex systems which are composed of several interfaces. A high level of electron accumulation must occur because photogenerated electrons are not extracted immediately at the electrode contact under illumination. Generally, the impedance at low frequency (0.05–1 Hz) refers to the Nernst diffusion of I_3^-/I^- within the electrolyte. The impedance at high frequency (1–100 kHz) corresponds to the capacitance and charge-transfer resistance at the Pt|I_3^-/I^- electrolyte interface. The medium-frequency response at 1 Hz–100 Hz is related to the photoelectrode–dye|I_3^-/I^- electrolyte interface, where the accumulation of photoelectrons and redox shuttles is expected[32,33]. Figure 10 shows the EIS of pure TiO_2 cell and TiO_2-Bi_2S_3:Eu^{3+} cell. It can be seen

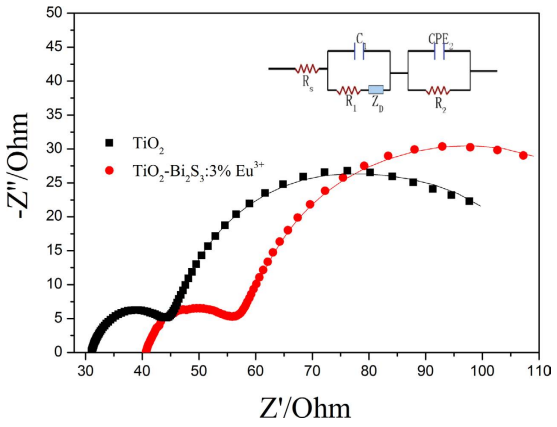

Figure 10. Nyquist plots of DSSCs comprised of pure TiO_2 cell and TiO_2-3%Bi_2S_3:Eu^{3+} cell. Inset is the equivalent circuit used to represent interfaces in composite solar cells composed of FTO|TiO_2-dye|I^-/I^{3-}||Pt|FTO.

DSSCs	R_s/Ω	C_1/F	R_1/Ω	Y_{o1}/S	$B/s^{1/2}$	R_2/Ω	CPE
Pure TiO_2	31.53	9.378×10^{-6}	12.00	0.01077	0.387	30.31	0.0005914
TiO_2-Bi_2S_3:3%Eu^{3+}	41.26	7.789×10^{-6}	12.30	0.00641	0.252	41.30	0.00217

Table 2. Parameters obtained by fitting the impedance spectra of composite solar cells using the equivalent circuit in the inset of Fig. 9.

that the interfacial resistance of the TiO_2-dye|I_3^-/I^- electrolyte interface of TiO_2-Bi_2S_3:Eu^{3+} cell is much bigger than that of pure TiO_2 cell.

The inset in Fig. 10 shows the equivalent circuit fitting of the impedance spectra, $R_s[C_1(R_1O_1)](R_2CPE)$, which was used for all the DSSCs. R_s is the series resistance, corresponding to the sheet resistance of the FTO glass, the contact resistance and the wire resistance. R_2 represents the charge transfer resistance between the photoelectrode-dye|I_3^-/I^- electrolyte interface. Z_{Dif} represents the finite-length Warburg impedance. The impedance of the finite-length Warburg diffusion is expressed as $Z_{Dif} = R_{Dif}\frac{\tanh(j\omega\tau)^{1/2}}{(j\omega\tau)^{1/2}}$ where $R_{Dif} = B/Y_0$, and $\tau = B^2$. B is a constant phase element.

According to the equivalent circuit, the EIS data obtained by fitting the impedance spectra of composite DSSCs are listed in Table 2. It can be seen that R_2, representing the interfacial resistance of the TiO_2-dye|I_3^-/I^- electrolyte interface, is 30.31 Ω for pure TiO_2 cell and 41.30 Ω for TiO_2-Bi_2S_3:Eu^{3+} composite cell. It is noted that the lower interfacial resistance can result in higher interfacial electron transfer, which is a beneficial factor for enhanced photoelectric conversion efficiency. In addition, the series resistance (R_S) for pure TiO_2 cell and TiO_2-Bi_2S_3:Eu^{3+} cell are separately 31.53 Ω and 41.26 Ω, indicating that the incorporation of Bi_2S_3:Eu^{3+} is not beneficial for the interfacial electron transfer of FTO|TiO_2.

In DSSCs, the electron recombination time (τ_n), the electron transport time (τ_d), and the charge collection efficiency (η_{cc}) are important factors for the performance of DSSCs. Time-resolved photoluminescence spectrum can be used as an effective method to characterize the interface electron transport and electron recombination of the solar cell[34,35]. But restricted by the conditions, we can not test Time-resolved photoluminescence spectrum. However, the IMVS and IMPS are also a kind of effective characterization methods, which can be used to characterize the transmission life, charge separation and recombination of interface electrons. The IMPS response plots and IMVS response plots of pure TiO_2 cell and TiO_2-Bi_2S_3:Eu^{3+} composite cell are shown in Fig. 11. Compared with pure TiO_2 cell, the TiO_2-Bi_2S_3:Eu^{3+} composite cell has longer electron recombination time and longer electron transport time. It noted that longer transport time can result in poorer photoelectric properties, while longer recombination time is beneficial for enhancing photoelectric properties.

The charge collection efficiencies (η_{cc}) of DSSCs are determined by the relation: $\eta_{cc} = 1 - \tau_d/\tau_n$. Where, τ_d is a charge transport time and τ_n is a charge recombination lifetime. Figure 12 shows the charge collection efficiencies of pure TiO_2 cell and TiO_2-Bi_2S_3:Eu^{3+} cell. TiO_2-Bi_2S_3:Eu^{3+} composite cell has a higher charge collection efficiency than pure TiO_2 cell. All these results indicated that the performance of the solar cells can be improved by adding Bi_2S_3:Eu^{3+}.

In summary, flower-like Bi_2S_3:Eu^{3+} was successfully prepared by a facial solvothermal method. The obtained Bi_2S_3:Eu^{3+} was chosen to design TiO_2-Bi_2S_3:Eu^{3+} composite photoanodes. The result indicated that the photoelectric conversion efficiency were enhanced greatly by the incorporation of Bi_2S_3:Eu^{3+}. The best photoelectric conversion performance was observed when the mass concentration of Bi_2S_3:Eu^{3+} was 3 wt%. The result of EIS analysis revealed that the interfacial resistance of the TiO_2-dye|I_3^-/I^- electrolyte interface of TiO_2-Bi_2S_3:Eu^{3+} composite cell was much bigger than that of pure TiO_2 cell. In addition, the TiO_2-Bi_2S_3:Eu^{3+} composite cell exhibited longer electron recombination time, longer electron transport time, and higher charge collection efficiency than

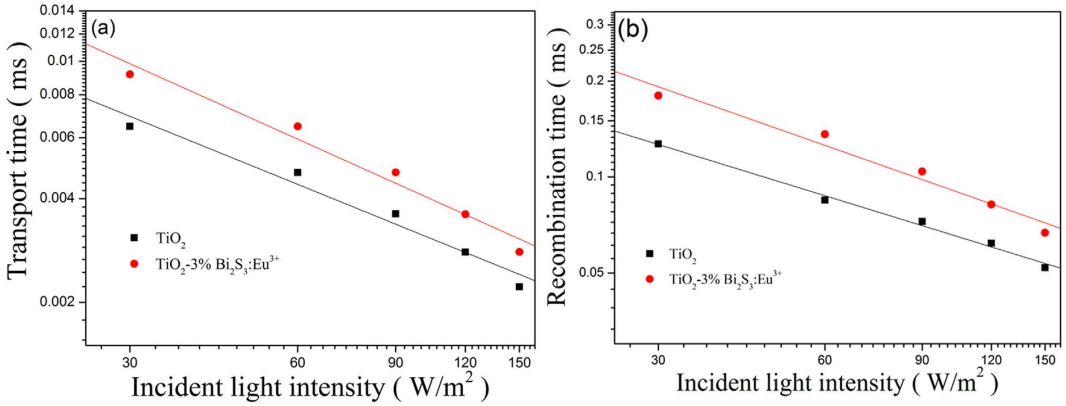

Figure 11. Comparison of (**a**) transport time constant and (**b**) recombination time constant for DSSCs comprised of pure TiO_2 cell and TiO_2-3%Bi_2S_3:Eu^{3+} cell.

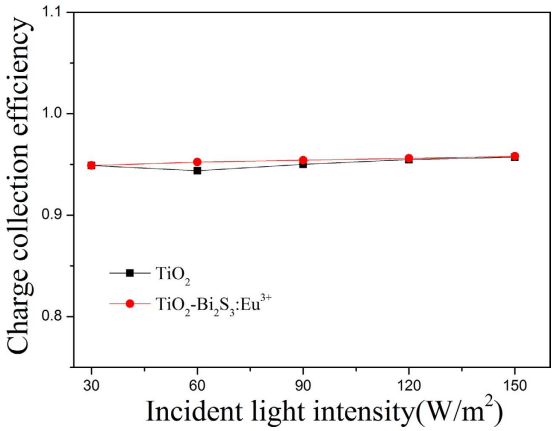

Figure 12. Comparison of charge collection efficiency for DSSCs comprised of pure TiO_2 cell and TiO_2-Bi_2S_3:Eu^{3+} cell.

those of pure TiO_2 cell. Of course, the enhancement of the efficiency of the TiO_2-Bi_2S_3:Eu^{3+} composite cells was also related to the larger BET surface areas of Bi_2S_3:Eu^{3+}.

Methods

Synthesis of flower-like Bi_2S_3 nanocrystals. In a typical experiment, $Bi(NO_3)_3$, CH_4N_2S and $Eu(NO_3)_3$ were separated add to ethylene glycol (10 ml), and the solution was thoroughly stirred. Subsequently, the solution was transferred to a 50 ml Teflon-lined autoclave for 12 h at 180 °C. After cooling to room temperature, the final products were collected by means of centrifugation, washed with ethanol, dried at 80 °C in air and then annealed at different temperature.

Fabrication of photoelectrodes. Fabrication of photoelectrode and the assembly of DSSCs: several pastes, from homogeneously mixing Bi_2S_3:Eu^{3+} and TiO_2 (Degussa P25) into 3 mL of TiO_2 colloid, were prepared with different mass concentrations of Bi_2S_3:Eu^{3+}. The TiO_2 colloid was prepared following the previously published synthesis procedure[36]. A screen-printed double layer of TiO_2-Bi_2S_3:Eu^{3+} was used as the photoanode. The first layer of TiO_2-Bi_2S_3:Eu^{3+} was prepared by a doctor-blade method on the FTO substrate and then sintered at 450 °C for 1 h. Subsequently, the second layer of TiO_2-Bi_2S_3:Eu^{3+} was covered on the first TiO_2-Bi_2S_3:Eu^{3+} film and then sintered at 450 °C for 30 min again. The sensitization of the photoelectrodes was achieved by immersing them into 0.5 mM $((C_4H_9)_4N)_2$[Ru(4-carboxy-4′-carboxylate-2,2′ bipyridine)2$(NCS)_2$] dye (N719, Solaronix SA, Switzerland) in acetonitrile and tertbutanol (volume ratio, 1:1) for 48 h at room temperature. The Pt counter electrodes were prepared following the previous literature[37]. The dye-sensitized photoanode was assembled with a Pt counter electrode into a sandwichtype cell. The sandwich-type cell was further fixed together with epoxy resin.The space between the electrodes was filled with the electrolyte, which comprised 0.6 M 1-propyl-2,3 -dimethyl-imidazolium iodide, 0.05 M I_2, 0.1 M LiI, and 0.5 M tert-butylpyridine (TBP) in 3-methoxypropionitrile (3-MPN), by capillary action.

Materials Characterizations. The composition of the materials was determined by a Rigaku (Japan) D/MAX-rA X-ray diffraction meter (XRD) equipped with graphite monochromatized Cu Kα radiation

($\gamma = 1.541874$ Å), keeping the operating voltage and current at 40 kV and 40 mA. The size and morphology of the final products were investigated by scanning electron microscopy (SEM, Hitachi, S-4800) and transmission electron microscopy (TEM, JEOL, JEM-3010). UV-Vis absorption spectrum were determined by a UV–Vis spectrophotometer (Shimadzu UV-2550, Tokyo, Japan). The Raman spectra were measured by a HORIBA JOBIN YVON LabRam-HR 800 micro-Raman spectrometer.

Photovoltaic properties study. Photovoltaic measurements were carried out with a solar simulator (Oriel, USA) equipped with an AM 1.5G radiation (1 sun conditions, 100 mW cm^{-2}) filter was used as the light source. Current-voltage (J–V) curves were measured with a BAS100B electrochemical analyzer (Zahner Elektrik, Germany). The area of DSSCs is 1.5 cm^2 and the irradiation area is 0.09 cm^2 with a light intensity meter. The photoanode of Bi_2S_3:Eu^{3+} films were fabricated in the same condition. To make the data strictly and scientifically, all the cells was test for at least 5 times then obtained an average value. The EIS were performed with a computer-controlled IM6e impedance measurement unit (Zahner Elektrik, Germany) and carried out by applying sinusoidal perturbations of 10 mV with a bias of −0.8 V at a frequency ranges from 10 mHz to 1 MHz. The obtained spectra were fitted with ZsimpWin software in terms of appropriate equivalent circuits. The electron transport and recombination properties were measured by intensity-modulated photocurrent spectroscopy (IMPS) and intensity-modulated photovoltage spectroscopy (IMVS) (Zahner Elektrik, Germany). The DSSCs were probed through the photoanode side by a frequency response analyzer using a white lightemitting diode (wlr-01) as the light source. The frequency range was 0.1–1000 Hz. The irradiated intensity was varied from 30 to 150 mW cm^{-2}.

References

1. O'Regan, B. & Gr¨atzel, M. A low-cost, high-efficiency solar cell based on dye-sensitized colloidal TiO_2 films. *Nature* **353,** 737–740 (1991).
2. Kung, C. W. *et al.* CoS acicular nanorod arrays for the counter electrode of an efficient dye-sensitized solar cell. *ACS Nano* **6,** 7016–7025 (2012).
3. Miao, X. H. *et al.* Well-dispersed CoS nanoparticles on a functionalized graphene nanosheet surface: A counter electrode of dye-sensitized solar cells. *Chem. - Eur. J.* **20,** 474–482 (2014).
4. Choi, H. *et al.* High molar extinction coefficient organic sensitizers for efficient dye-sensitized solar cells. *Chem.-Eur. J.* **16,** 1193–1201 (2010).
5. Luo, Y., Li, D. & Meng, Q. Towards optimization of materials for dye-sensitized solar cells. *Adv. Mater.* **21,** 4647–4651 (2009).
6. Song, J. G., Song, X., Ling, T., Du, X. W. & Qiao, S. Z. Enhancing the conversion efficiency of semiconductor sensitized solar cells via the co-sensitization of dual-sized quantum dots. *Ind. Eng. Chem. Res.* **51,** 10074–10078 (2012).
7. Du, J., Qi, J., Wang, D. & Tang, Z. Y. Facile synthesis of Au@TiO_2 core-shell hollow spheres for dye-sensitized solar cells with remarkably improved efficiency. *Energy Environ. Sci.* **5,** 6914–6918 (2012).
8. Choi, H. *et al.* An efficient dye-sensitized solar cell with an organic sensitizer encapsulated in a cyclodextrin Cavity. *Angew. Chem.-Int. Edit.* **48,** 5938–5941 (2009).
9. Choi, H. *et al.* Highly efficient and thermally stable organic sensitizers for solvent-free dye-sensitized solar cells. *Angew. Chem.- Int. Edit.* **47,** 327–330 (2008).
10. Li, Q. H. *et al.* Reducing the excess energy offset in organic/inorganic hybrid solarcells: Toward faster electron transfer. *Appl. Catal. B-Environ.* **162,** 524–531 (2015).
11. Jin, X. *et al.* Exciton generation/dissociation/charge-transfer enhancement in inorganic/organic hybrid solar cells by robust single nanocrystalline LnP_xO_y (Ln = Eu, Y) Doping. *ACS Appl. Mater. Inter.* **6,** 8771–8781 (2014).
12. Chen, X. X. *et al.* Platinum-free binary Co-Ni alloy conter electrodes for efficiet dye-sensitised solar cells. *Angew. Chem.- Int. Edit.* **53,** 10799–10803 (2014).
13. Duan, Y. Y. *et al.* Transparent metal selenide alloy counter electrodes for high-efficiency bifacial dye-sensitized solar cells. *Angew. Chem.- Int. Edit.* **53,** 14569–14574 (2014).
14. Wang, Z. B. *et al.* Recent advances in alloy counter electrodes for dye-sensitized solar cells. A critical review. *Electrochim. Acta* **178,** 886–899 (2015).
15. Tang, Q. W. *et al.* Dissolution engineering of platinum alloy counter electrodes in dye-sensitized solar cells. *Angew. Chem.- Int. Edit.* **54,** 11448–11452 (2015).
16. Liao, Y. P. *et al.* Facile synthesis of high-crystallinity graphitic carbon/Fe_3C nanocomposites as counter electrodes for high-efficiency dye-sensitized solar cells. *ACS Appl. Mater. Inter.* **5,** 3663–3670 (2013).
17. Huang, X. Y., Han, S. Y., Huang, W. & Liu, X. G. Enhancing solar cell efficiency: the search for luminescent materials as spectral converters. *Chem. Soc. Rev.* **42,** 173–201 (2013).
18. Wang, Q., Gao, R. & Li, J. H. Porous, self-supported Ni_3S_2/Ni nanoarchitectured electrode operating through efficient lithium-driven conversion reactions. *Appl. Phys. Lett.* **90,** 143107 (2007).
19. Hardin, B. E. *et al.* Increased light harvesting in dye-sensitized solar cells with energy relay dyes. *Nat. Photonics* **3,** 406–411 (2009).
20. Brahimi, R., Bessekhouad, Y., Bouguelia, A. & Trari, M. Visible light induced hydrogen evolution over the heterosystem Bi_2S_3/TiO_2. *Catal. Today* **122,** 62–65 (2007).
21. Liao, H. C. *et al.* Synthesis, optical and photovoltaic properties of bismuth sulfide nanorods. *CrystEngComm* **14,** 3645–3652 (2012).
22. Grigas, J., Talik, E. & Lazauskas, V. X-ray photoelectron spectra and electron structure of Bi_2S_3 crystals. *Phys. Status Solidi.* **232,** 220–230 (2002).
23. Phuruangrat, A., Thongtem, S. & Thongtem, T. Controlling morphologies of Bi_2S_3 nanostructures synthesized by glycothermal method. *Mater. Lett.* **72,** 104–106 (2012).
24. Dong, Z. *et al.* Accurate control of multishelled ZnO hollow microspheres for dye-sensitized solar cells with high efficiency. *Adv. Mater.* **24,** 1046–1049 (2012).
25. Gao, C., Shen, H. L., Sun, L. & Shen, Z. Chemical bath deposition of Bi_2S_3 films by a novel deposition system. *Appl. Sur. Sci.* **257,** 7529–7533 (2011).
26. Wang, S. Y. & Du, Y. W. Preparation of nanocrystalline bismuth sulfide thin films by asynchronous-pulse ultrasonic spray pyrolysis technique. *J. Cryst. Growth* **236,** 627–634 (2002).
27. Wu, J. L., Qin, F. & Cheng, G. Large-scale synthesis of bismuth sulfide nanorods by microwave irradiation. *J. Alloy. Compd.* **509,** 2116–2126 (2011).
28. Zhang, H., Huang, J., Zhou, X. G. & Zhong, X. H. Single-crystal Bi_2S_3 nanosheets growing via attachment-recrystallization of nanorods. *Inorg. Chem.* **50,** 7729–7734 (2011).
29. Yang, X., Wang, X. & Zhang, Z. Facile solvothermal synthesis of single-crystalline Bi_2S_3 nanorods on a large scale. *Mater. Chem. Phys.* **95,** 154–157 (2006).

30. Lan, J. L. *et al.* Effects of iodine content in the electrolyte on the charge transfer and power conversion efficiency of dye-sensitized solar cells under low light intensities. *J. Phys. Chem. C* **116,** 25727–25733 (2012).
31. Qian, J. *et al.* TiO_2-coated multilayered SnO_2 hollow microspheres for dye-sensitized solar cells. *Adv. Mater.* **21,** 3663–3667 (2009).
32. Longo, C., Nogueira, A. F., De Paoli, M. A. & Cachet, H. Solid-state and flexible dye-sensitized TiO_2 solar cells: a study by electrochemical impedance spectroscopy. *J. Phys. Chem. B* **106,** 5925–5930 (2002).
33. Zhang, J. Y. *et al.* Ligand-assisted assembly approach to synthesize large-pore ordered mesoporous titania with thermally stable and crystalli framework. *Adv. Energy Mater.* **1,** 241–248 (2011).
34. Li, Q. H. *et al.* $Nd_2(S, Se, Te)_3$ colloidal quantum dots: synthesis, energy level alignment, charge transfer dynamics, and their applications to solar cells. *Adv. Funct. Mater.* **26,** 254–266 (2016).
35. Jin, X. *et al.* Energy gradient architectured praseodymium chalcogenide quantum dot solar cells: towards unidirectionally funneling energy transfer. *J. Mater. Chem. A.* **3,** 23876–23887 (2015).
36. Yang, J. *et al.* High catalytic activity and stability of nickel sulfide and cobalt sulfide hierarchical nanospheres on the counter electrodes for dye-sensitized solar cells. *Chem. Commun.* **50,** 4824–4826 (2014).
37. Li, Y. B. *et al.* A {0001} faceted single crystal NiS nanosheet electrocatalyst for dye-sensitised solar cells: sulfur-vacancy induced electrocatalytic activity. *Chem. Commun.* **50,** 5569–5571 (2014).

Acknowledgements

We gratefully acknowledge the support of this research by the National Natural Science Foundation of China (21471050), Program for Innovative Research Team in University (IRT-1237), Innovation Team of Education Bureau of Heilongjiang Province (2013TD002), and Heilongjiang Province Natural Science Foundation of Key Projects (ZD201301).

Author Contributions

B.Y.X. performed synthesis experiments, G.F.W. and H.G.F. designed the experiment. G.F.W. carried out photo-electrochemical evaluation and discussion. B.Y.X. and G.F.W. wrote the manuscript.

Additional Information

Competing financial interests: The authors declare no competing financial interests.

How to cite this article: Xu, B. *et al.* 23327Enhanced photoelectric conversion efficiency of dye-sensitized solar cells by the incorporation of flower-like Bi_2S_3:Eu^{3+} sub-microspheres. *Sci. Rep.* **6**, 23395; doi: 10.1038/srep23395 (2016).